

The Influence of High-Frequency Atmospheric Forcing on the Circulation and Deep Convection of the Labrador Sea

AMBER M. HOLDSWORTH AND PAUL G. MYERS

Department of Earth and Atmospheric Sciences, University of Alberta, Edmonton, Alberta, Canada

(Manuscript received 12 August 2014, in final form 20 March 2015)

ABSTRACT

The influence of high-frequency atmospheric forcing on the circulation of the North Atlantic Ocean with emphasis on the deep convection of the Labrador Sea was investigated by comparing simulations of a coupled ocean–ice model with hourly atmospheric data to simulations in which the high-frequency phenomena were filtered from the air temperature and wind fields. In the absence of high-frequency atmospheric forcing, the strength of the Atlantic meridional overturning circulation and subpolar gyres was found to decrease by 25%. In the Labrador Sea, the eddy kinetic energy decreased by 75% and the average maximum mixed layer depth decreased by between 20% and 110% depending on the climatology. In particular, high-frequency forcing was found to have a greater impact on mixed layer deepening in moderate to warm years whereas in relatively cold years the temperatures alone were enough to facilitate deep convection. Additional simulations in which either the wind or temperature was filtered revealed that the wind, through its impact on the bulk formulas for latent and sensible heat, had a greater impact on deep convection than the temperature.

1. Introduction

The Labrador Sea is a region where significant coupling between the atmosphere and ocean occurs. Mediated by the strength of the subpolar gyre, persistent winds and extreme winter temperatures can trigger the formation of deep convecting plumes with radii ≤ 1 km (Marshall and Schott 1999) that mix the water column down to 2 km (Lazier 1980; Lilly et al. 2003). When this happens chemicals and energy are exchanged between the lower atmosphere and the interior of the ocean.

In the surface mixed layer biogeochemicals such as carbon dioxide (CO_2), chlorofluorocarbons (CFCs), tritium (^3H), and oxygen (O_2) are close to equilibrium with atmospheric concentrations. But cooler abyssal waters are naturally depleted of O_2 by marine life and have a larger capacity for storing CO_2 . Deep convection replenishes abyssal O_2 concentrations and injects anthropogenic CO_2 in the intermediate layers (Azetsu-Scott et al. 2003). This ventilates the waters of the Labrador

Sea, facilitating the rise of nutrient-rich waters that stimulate the local ecosystem.

Lateral mixing of deeply convected fluid forms a weakly stratified patch of Labrador Seawater (LSW). The density of this water mass varies from year to year depending on oceanic advection, stratification, air–sea fluxes, and preconditioning (Myers and Donnelly 2008). Preconditioning is the weakening of the stratification of the water column prior to deep convection and is facilitated by a concert of factors—for example, the strengthening of the cyclonic gyre that results in a convex doming of isopycnals, the presence of LSW from previously convected winters, or an increase in high-frequency forcing (Marshall et al. 1998; Condron and Renfrew 2013). Changes in surface forcing due to cold air outbreaks, polar lows, or storms may induce deep convection (Marshall and Schott 1999) or act to precondition the sea for convection depending on when they form. The extent of mixed layer deepening in the Labrador Sea has consequences for the strength and shape of the Atlantic meridional overturning circulation (AMOC) (Kuhlbrodt et al. 2007).

The Labrador and Greenland Seas are the primary locations in the northern oceans where deep convection takes place (Marshall and Schott 1999). Through many different mechanisms, the deep water that forms in these regions is transported south where it upwells.

Corresponding author address: Amber M. Holdsworth, Department of Earth and Atmospheric Sciences, University of Alberta, Edmonton, AB T6G 2G7, Canada.
E-mail: aholdsw@ualberta.ca

Concomitantly, warm surface waters from midlatitudes are transported poleward, forming a branch of the deep overturning circulation known as the AMOC. A combination of factors is thought to drive the AMOC including the winds, buoyancy forcing at the surface, and mechanical mixing throughout the ocean interior, but efforts to understand these processes are ongoing (Wunsch and Ferrari 2004; Kuhlbrodt et al. 2007; Ferrari and Wunsch 2009; Nikurashin et al. 2013).

In the last decade, observations of the AMOC have improved as the Rapid Climate Change (RAPID) program continuously observes the strength and structure of the AMOC at 26.5°N. Rayner et al. (2011) show that in the first year of deployment large variability in the AMOC was observed with changes on seasonal, monthly, and weekly time scales. Internal waves and eddies are cited as possible sources of the variability; however, the mechanisms responsible for these high-frequency oscillations are not well understood. High-frequency atmospheric forcing has the potential to influence these processes (Polo et al. 2014; Xu et al. 2014).

While extreme convection in excess of 2 km has not been observed since the 1990s (Avisic et al. 2006), extreme convection was observed in the winter of 2007/08 without any sign of preconditioning from the previous year (Våge et al. 2009). Climatological conditions were cited as the predominant factor contributing to the return of deep convection in 2008 (Yashayaev and Loder 2009), but the enhanced deep convection of 2008 was shown to be influenced by a concert of factors including storms, freshwater fluxes, and the distribution of the ice pack. Våge et al. (2009) argued that even a moderate shift in storm tracks could have profound consequences for deep convection in both the Greenland and the Labrador Seas. Yet the influence of climatological factors relative to the influence of high-frequency atmospheric phenomena remains unclear.

Several studies have examined the influence of storms on the circulation of the North Atlantic Ocean (Condrón and Renfrew 2013; Jung et al. 2014). While they do not focus on the Labrador Sea in particular, these studies are relevant to a discussion of the role of high-frequency forcing on deep convection and ocean circulation. Now, we briefly describe the pertinent findings of these studies.

Condrón and Renfrew (2013) examined the impact of polar mesoscale storms on the circulation of the North Atlantic Ocean. They compared simulations forced with and without a parameterization of polar lows and showed that these storms contribute to the volume of Greenland Sea Deep Water (GSDW) as well as influencing the frequency, depth, and area of deep convection (Condrón et al. 2006; Condrón and Renfrew 2013).

Jung et al. (2014) have shown that small-scale atmospheric forcing phenomena including mesoscale cyclones,

fronts, and topographic jets play an important role in driving the mean ocean circulation. They isolated the pure effect of resolution by coarse-graining their atmospheric forcing data and running the model at relatively high and low resolutions. They found that mesoscale phenomena strengthened the mean horizontal wind-driven ocean circulation by about 5%–10%. Hence, the relatively coarse resolution typically implemented in global climate models inevitably results in an underestimate of the AMOC and wind-driven circulations.

Luo et al. (2014) used a similar approach to investigate the effect of changing the temporal resolution on deep convection in the Labrador Sea and suggested that a detailed representation of extreme winter events is not necessary if their average impacts are accounted for. However, their study focused on obtaining a realistic representation of observations while constraining the model drift and, thus, implemented nudging to a monthly surface salinity climatology, which may have biased the model away from extreme events. For this reason, our study does not implement surface restoring.

Most studies investigating the influence of high-frequency forcing on the ocean have used atmospheric forcing data with a resolution of 6 h (Jung et al. 2014; Luo et al. 2014). However, Roberts et al. (2015) demonstrated the importance of frequent atmosphere–ice–ocean coupling in simulating ice–ocean Ekman transport and suggested that, because of the limitations of the Nyquist frequency, a tightly synchronized coupling is the most important model mechanism required to simulate high-frequency ice mechanics. As a result a high temporal resolution is prerequisite to an investigation of high-frequency atmospheric forcing.

We explore the role of high-frequency atmospheric forcing on the circulation of the North Atlantic Ocean with particular focus on the deep convection of the Labrador Sea. To our knowledge, this study is the first to use hourly atmospheric forcing that resolves a wide range of atmospheric phenomena to investigate the influence of high-frequency forcing. We compare simulations of an ocean–ice coupled model forced with high-resolution data to simulations in which high-frequency atmospheric phenomena have been removed. Since the Labrador Sea is vital to our global climate system, understanding the role that high-frequency atmospheric forcing plays there will help to indicate the significance of high-frequency forcing to global ocean circulation.

In section 2, we describe the model and the relevant data including the filtration process. Section 3 describes our analysis methods; the results of this analysis are presented in section 4. Finally, a discussion and conclusions are presented in section 5.

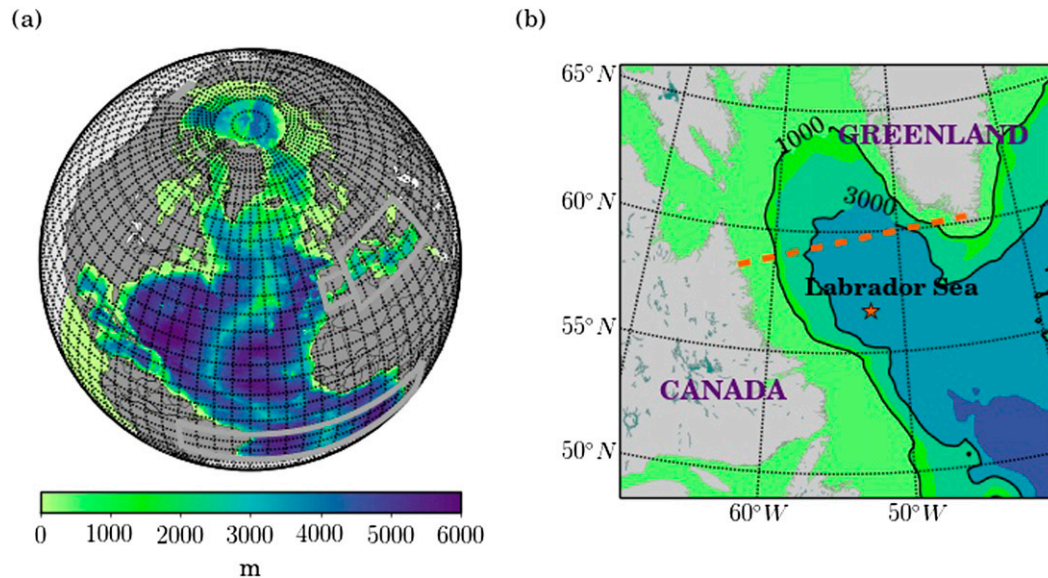


FIG. 1. The bathymetry over the (a) domain of ANHA4 and (b) Labrador Sea. Buffer zones are indicated with light gray squares and orange markings indicate relevant locations referred to in the text.

2. Model description and data

a. Ocean–ice model

We used the Nucleus for European Modelling of the Ocean, version 3.1 (NEMO v3.1) (Madec 2008). The Arctic Northern Hemisphere Atlantic configuration (ANHA4) shown in Fig. 1 was based on the 0.25° tripolar grid extracted from the NEMO ORCA025 configuration developed within the Mercator Océan and DRAKKAR collaboration (Barnier et al. 2007). The model consists of 50 vertical levels with a 1-m top layer decreasing in resolution with increasing depth. The ANHA4 domain is contained within open boundaries at 20°S latitude and the Bering Strait as shown in Fig. 1. Lateral boundaries are free slip with buffer zones indicated on the figure with light gray squares.

Lateral mixing varies horizontally according to a bi-Laplacian operator with a horizontal eddy viscosity of $3 \times 10^{11} \text{ m}^4 \text{ s}^{-1}$. For tracer lateral diffusion, the model uses an isopycnal Laplacian operator with a horizontal eddy diffusivity of $300 \text{ m}^2 \text{ s}^{-1}$.

Vertical mixing at subgrid scales was parameterized using a second-order turbulent closure scheme based on the turbulent kinetic energy (Mellor and Yamada 1982). Background vertical eddy viscosity and diffusivity are 10^{-4} and $10^{-5} \text{ m}^{-2} \text{ s}^{-1}$, respectively.

Eddies in the Labrador Sea range in size with radii between 5 and 30 km (Lilly et al. 2003). So the model is eddy permitting, but the resolution is not fine enough to resolve all of the eddies (Hallberg 2013).

The NEMO model is coupled with the Los Alamos Sea Ice Model (CICE; Hunke and Lipscomb 2008). The Co-ordinated Ocean–Ice Reference Experiments (CORE) bulk formulas were applied to compute fluxes of heat, water, and momentum (Large and Yeager 2009).

b. Input data

The simulations presented here were forced with interannual atmospheric data. Our control experiment used data derived from the Canadian Meteorological Centre's global deterministic prediction system reforecasts (CGRF; Smith et al. 2014) with an hourly resolution in time and a spatial resolution of 0.45° longitude and 0.3° latitude ($\approx 33 \text{ km}$ in the Labrador Sea). This dataset was produced by rerunning the current numerical weather prediction analysis system over the period from 2002 to 2010. For each day, the forecast was run for 30 h and the first 6 h were rejected to allow the model dynamics to spin up. Although the CGRF are not as tightly constrained to fit with observations as available reanalysis products such as ERA-Interim, Smith et al. (2014) demonstrated that CGRF has comparable biases in terms of the surface temperature, humidity, and winds. The relatively high resolution permits a more detailed representation of atmospheric structures at high latitudes (Smith et al. 2014). Therefore, the CGRF data are well suited to the present examination of high-frequency atmospheric phenomena.

The Co-ordinated Ocean–Ice Reference Experiments with interannually varying atmospheric forcing (CORE-II; Large and Yeager 2004, 2009) dataset was developed to provide a common framework for evaluating the

behavior of global ocean–ice coupled simulations. So we also ran simulations forced with CORE-II data for comparison. The relevant fields have a 6-hourly resolution in time and a spatial resolution of about 1.9° (~ 100 km in the Labrador Sea).

Common inputs used in both the CGRF and CORE-II simulations include the CORE-II snow data, the river runoff taken from the 12-month climatological data of Dai and Trenberth (2002), and the bathymetry derived from 1-minute gridded elevations/bathymetry for the world (ETOPO1) data (Amante and Eakins 2009) illustrated in Fig. 1. The simulations were initialized with Global Ocean Reanalyses and Simulations (GLORYS) data, allowed to spin up for 3 years, and then run from 2002 to 2010. The same data were also used for the buffer zones at the open boundaries.

Kolmogorov–Zurbenko (KZ) filtering is a well-established method for separating meso- and synoptic-scale meteorological data (Overland et al. 1999; Ibarra-Berastegi et al. 2001; Wise and Comrie 2005). Wavelet and KZ filtering are the most accurate and widely used low-pass filters for this purpose. We chose KZ filtering because it is straightforward to implement and has the distinct advantage that it can handle gaps in the data without having to interpolate between existing data points (Eskridge et al. 1997). For each point y_i , the KZ-filtered data are given by an iterative moving average over a window of length $D = 2q + 1$ so that

$$y_i = \frac{1}{2q + 1} \sum_{j=-q}^q y_{i+j} \quad (1)$$

is the input for the next iteration. The window is symmetric about the point i , so j ranges over q time steps prior to and after i .

Eskridge et al. (1997) predicted that the algorithm would filter scales of motion $DI^{1/2} \leq P$ days for I iterations. However, wavelet spectral analysis revealed that, for our relatively high-resolution dataset, the algorithm filters shorter time scales than predicted. For example, when $D = 10$ days and $I = 4$ iterations, scales below about 7 days are removed from the time series.

High-frequency atmospheric forcing phenomena manifest as short-time-scale changes in pressure, temperature, and wind stress. Each of these perturbations can lead to changes in heat flux but, quantitatively speaking, the associated change in heat flux is not readily identifiable. Thus, we expect that filtering such phenomena from our forcing data will reduce the climatological mean; however, it is not clear how much of a reduction is appropriate. Hence, we chose a window of $D = 10$ days and $I = 4$ iterations so that all of the forcing acting over time periods of one week or less were removed

while minimizing the reduction of mean values. Over the entire domain, the mean values of the temperature and wind speeds for the unfiltered data were \bar{T} of 284 K and \bar{S} of 5.3 m s^{-1} and for the filtered data we have \bar{T} of 284 K and \bar{S} of 3.7 m s^{-1} . Reviewing animations of the filtered temperature and wind fields for the unfiltered and filtered forcing fields verified that the majority of cyclones were removed from the wind and temperature fields.

In the Northern Hemisphere less than 17% of cyclones last for more than 7 days (Gulev et al. 2001) with most cyclones in the Atlantic region lasting between 2 and 6 days and Arctic cyclones living an average of 3 days. Therefore, filtering all wind and temperature perturbations lasting less than one week is sufficient to explore the influence of high-frequency atmospheric forcing on deep convection and ocean circulation.

The filter removed temperature and wind perturbations occurring over mesoscale time periods such as storms, as well as other atmospheric phenomena including barrier winds, fronts, and topographic jets like the Greenland tip jet and reverse tip jet (Moore and Renfrew 2005).

Figure 2e shows the time series from 2002 to 2010 extracted from the CGRF temperature data at the location of the Atlantic repeat hydrography line 7 west (AR7W) Bravo mooring site shown as an orange star in Fig. 1 (56.75°N , 52.5°W ; Lilly et al. 2003). Despite the fact that domain averaged temperatures were the same for both filtered and unfiltered forcing, there are significant differences between the filtered and unfiltered time series shown in Figs. 2e and 2f. In particular, local extrema have been removed. Winter temperatures reach extremes between -5° and -10°C every year. But in the filtered time series the winter of 2007/08 was the only winter which exhibited temperatures below -5°C as demonstrated by the dashed line in Fig. 2f. More broadly, we examined time series at several points in the interior of the Labrador Sea that confirmed that 2008 had more days with extremely cold air temperatures in comparison with the other years (not shown).

In Fig. 2g, the wavelet power spectrum shows the time–frequency spectrum of the filtered time series with the Fourier period on the y axis in place of the wavelet scale (see the appendix for a description of wavelet analysis). There is a peak in the spectrum at a period of less than one day spanning all of the years that reflects diurnal changes in temperature. Comparing Figs. 2g and 2h clearly shows that high-frequency atmospheric temperature perturbations have been removed.

Zonal and meridional components of the wind were filtered independently. For diagnostic purposes, we computed the wind stress curl as described by Smith (1988) from velocity time series extracted at the location

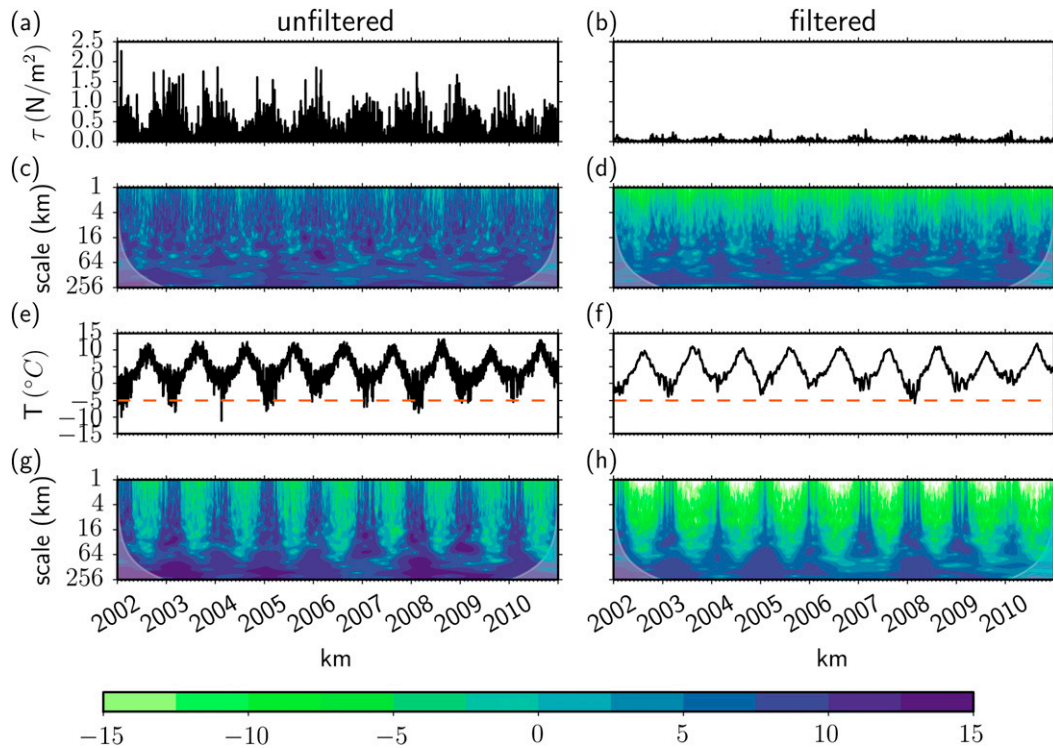


FIG. 2. Time series at the location of the orange star (Bravo) in Fig. 1 of (left) unfiltered and (right) filtered CGRF (a),(b) wind stress curl computed from the velocity fields at 10 m and (e),(f) 2-m air temperature. (c),(d) The corresponding wavelet power spectra for (a),(b). (g),(h) The corresponding wavelet power spectra for (e),(f). Color contours illustrate the magnitude of the wavelet coefficients and the light-shaded region illustrates the area outside the cone of influence which is unreliable. See the appendix for a more complete description.

of the orange star in Fig. 1. Wind stress time series are shown in Figs. 2a and 2b and corresponding wavelet power spectra shown in Figs. 2c and 2d demonstrate the effect of the low-pass filter. Figure 2c shows a seasonal pattern of recurring high-amplitude winds lasting a week or less, while in the filtered spectrum in Fig. 2d the high-frequency bursts of wind have been removed. This illustrates that the largest wind stresses occur over the shortest time scales.

We used wavelet spectral analysis to examine time series from several locations throughout the Labrador Sea. This confirmed that wind and temperature perturbations occurring over time scales of less than one week were effectively filtered from the CGRF atmospheric temperature and wind fields (not shown).

In the same manner, we applied wavelet spectral analysis to investigate the range of filtered spatial scales by extracting a series of values at a fixed latitude and across all longitudes. For example, Fig. 3 shows the wind stress and temperature extracted at 45°N. The wavelet power spectra shown in Figs. 3c, 3d, 3g, and 3h show that a wide range of spatial scales were removed.

Although the filter removed time periods consistent with the mesoscale, the range of geometries filtered extended to larger-scale atmospheric motions.

The average wintertime wind stress curl is shown in Fig. 4. The most significant differences observed between the unfiltered and filtered wind fields are along the North Atlantic and North Pacific storm tracks, near the Bering Strait, and near topographic features in the vicinity of Greenland.

The heat fluxes for unfiltered and filtered simulations are shown in Fig. 5. Removing high-frequency atmospheric phenomena from the wind and temperature fields reduced the magnitude of latent and sensible heat fluxes between the atmosphere and ocean because both quantities depend on the velocity of the wind through the bulk formulas (Large and Yeager 2009). The lowest wintertime temperatures in the filtered data were between 50% and 70% of that of the unfiltered data. The number of days during which the magnitude of the 2-m air temperature from the unfiltered data was lower than the minimum wintertime temperature from the filtered data ranged from 5 days in 2004 to 40 days in 2008.

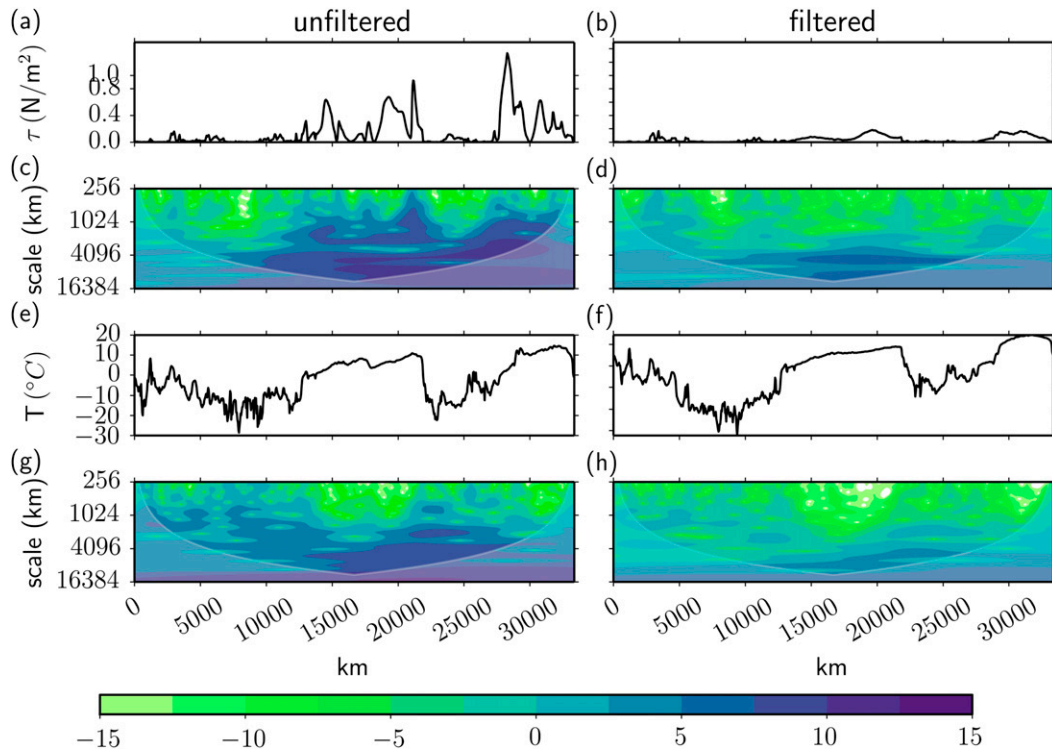


FIG. 3. Zonal series extracted at 45°N and across all latitudes of (left) unfiltered and (right) filtered CGRF (a),(b) wind stress curl at 10-m height and (e),(f) 2-m air temperature. (c),(d) The corresponding wavelet power spectra for (a),(b). (g),(h) The corresponding wavelet power spectra for (e),(f).

However, of those 40 days there were a maximum of 6 consecutive days during which the temperature was lower. Moreover, from 2002 to 2010 the temperature was lower for between 2 and 8 consecutive days. So the number of days over which the heat fluxes were reduced was consistent with the removal of high-frequency forcing, which provides further evidence

that the low-pass filter did not unduly reduce the climatological means.

3. Analysis methods

Time series of the Atlantic meridional overturning circulation was calculated at a fixed latitude ϕ and over all longitudes λ using

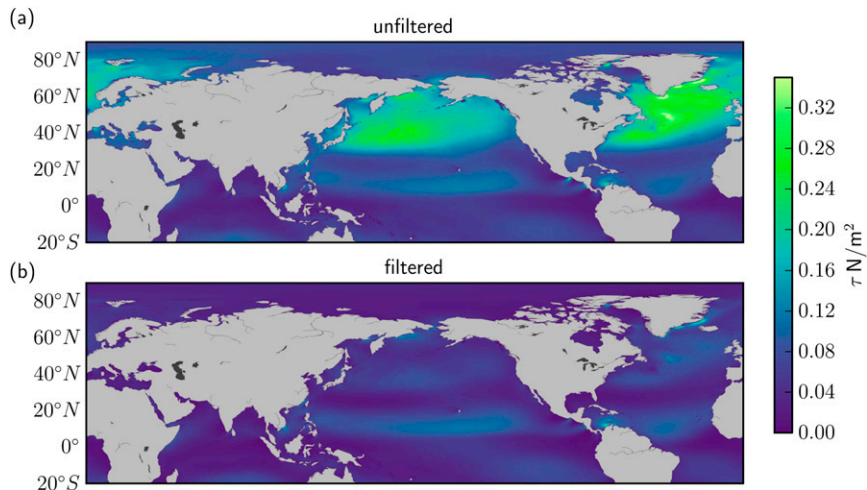


FIG. 4. Wind stress curl averaged over the Northern Hemisphere winter [January–March (JFM)].

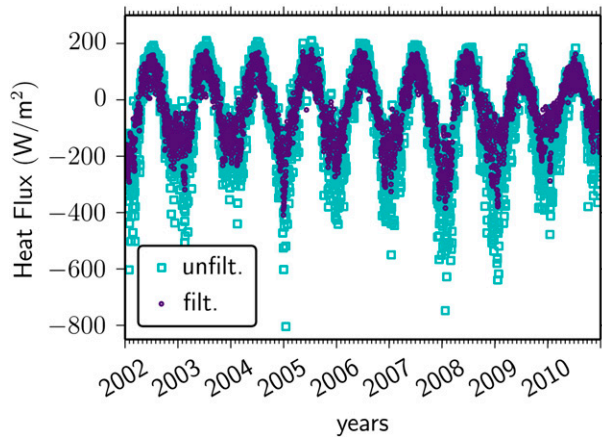


FIG. 5. Daily averaged heat flux computed using CORE bulk formulas within the 3000-m isobath of the Labrador Sea ($\lambda \leq 44^\circ\text{W}$).

$$\text{MOC}(h, \phi) = \int_h^0 \int_{\text{west}}^{\text{east}} v(\lambda, \phi, z, t) dx dz \quad (2)$$

at each depth h , where v is the meridional velocity, z is the vertical coordinate, and t is time.

The strength of the subpolar gyre was computed from the barotropic streamfunction. It can be shown that the volumetric flux between two streamlines is equivalent to the change in the streamfunction between those streamlines. Hence, by taking the maximum magnitude along a particular line connecting the coast of Greenland to the coast of Canada we obtained an estimate of the total volume transported by the subpolar gyre. We computed the climatological mean barotropic streamfunction for each day and found the minimum value along the section of the Labrador Sea indicated by the orange dashed line in Fig. 1b.

We defined the mixed layer depth (MLD) as the depth at which the density difference from the surface exceeded the threshold value of 0.01 kg m^{-3} . This value was chosen because observations indicate that the density of the mixed layer in the Labrador Sea varies by less than 0.01 kg m^{-3} (Lazier et al. 2002).

The stability of the water column depends not only on the surface mixed layer, but also on the density stratification of the water column. Thus, we provide a measure of the column stability to depths of 750 and 2000 m by quantifying the amount of energy per unit volume ($\text{kg m}^2 \text{ s}^{-1}$) required to mix the grid column to a depth h . The convective energy CE is defined by

$$\text{CE}(h) = \frac{g}{A} \iint_A \left[h \rho_{\text{pot}}(h) - \int_0^h \rho_{\text{pot}}(z) dz \right] dA, \quad (3)$$

where g is 9.81 m s^{-2} and A is the area of each grid cell. The potential density $\rho_{\text{pot}}(z)$ at each depth ($z < h$) is

compared to that of a well-mixed column of fluid with a density of $\rho_{\text{pot}}(h)$ to give the total amount of energy required to mix the column to a depth h . So $\text{CE}(h) = 0$ for a well-mixed fluid, $\text{CE}(h) > 0$ implies a stable density stratification, and $\text{CE}(h) < 0$ is indicative of an unstable density stratification. This quantity is derived from the concept of a buoyancy anomaly as described by Bailey et al. (2005) and Frajka-Williams et al. (2014).

Since the MLDs varied significantly between the filtered and unfiltered simulations, we normalized the values of the heat and freshwater content by dividing by the volume V of the mixed layer in each grid cell. Thus, the heat content (J m^{-3}) is given by

$$H = c_p \rho_0 \int_V (T - T_r) \frac{dV}{V}, \quad (4)$$

where c_p is the specific heat capacity of water, the reference density ρ_0 is 1020 kg m^{-3} , T is the model temperature, and the reference temperature T_r is 0°C . Similarly, the freshwater content is given by

$$\text{FW} = \int_V \frac{(S_r - S)}{S_r} \frac{dV}{V}, \quad (5)$$

where S is the model salinity and the reference salinity S_r is 35 ppt.

To obtain a single value for each day, values of MLD, CE, heat, and freshwater were averaged over the 3000-m isobath of the Labrador Sea extending as far east as 44°W . While this region is not indicated directly Fig. 1 shows the relevant bathymetry contours.

4. Results

a. Ocean circulation

Time series of the maximum AMOC taken at selected latitudes are shown in Fig. 6. The AMOC oscillates significantly in response to high-frequency atmospheric forcing. In particular, Table 1 shows the mean and standard deviation of the AMOC at 26.5°N from ANHA4 simulations and, for comparison, the RAPID observations. While the mean for the filtered run was closer to that of the RAPID array (Rayner et al. 2011), the unfiltered simulation more closely reproduced the variability of the observational data. That the standard deviation in the CORE-II simulations is comparable to the RAPID observations suggests that monthly smoothing does not completely obscure the influence of short-time-scale variability. The AMOC in the ANHA4 configuration is stronger, on average, than observations, which partially reflects the increasing trend, which is likely an artifact of model drift. While the unfiltered

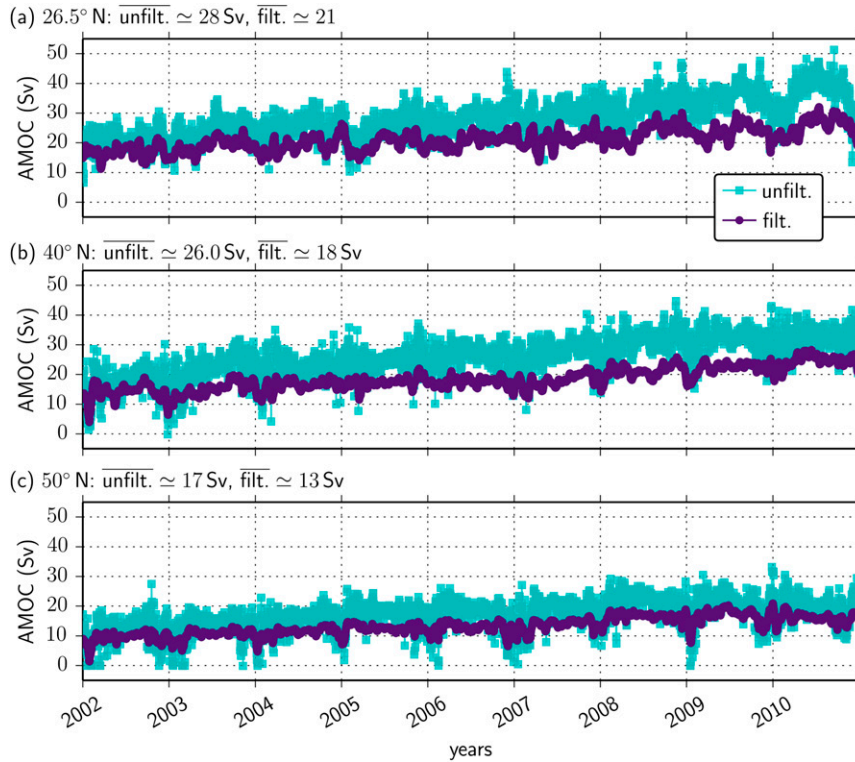


FIG. 6. Daily max AMOC [Eq. (2)] at selected latitudes.

simulation is more realistic in some ways, the associated air–sea fluxes are relatively large and may exacerbate model drift by introducing a positive feedback on deep convection. Over relatively short time periods, this does not detract from comparisons between the filtered and unfiltered runs. Averaging the increase across all of the latitudes in the figure, we found that the mean value of the AMOC decreased by about 25% when high-frequency atmospheric forcing was removed.

This result is significantly greater than that of Jung et al. (2014), who found that high-resolution atmospheric forcing increased the strength of the AMOC by 5%–10% on average over 20 years of integration. In agreement with their study, which showed that the response of the AMOC to an increase in high-frequency atmospheric forcing took several years to develop, we find that the difference between the strength of the AMOC in the filtered and unfiltered simulations increased in time.

Figure 7 shows the subpolar gyre strength for the filtered and unfiltered simulations. The high-frequency atmospheric forcing excited episodic spikes in subpolar gyre strength that were not present in the filtered simulation. This provides evidence that short-time-scale perturbations in the wind and temperature fields are responsible for the variability. The mean values of the gyre strength over this period were -52 Sverdrups (Sv;

$1 \text{ Sv} \equiv 10^6 \text{ m}^3 \text{ s}^{-1}$) with a standard deviation of 8 Sv for the unfiltered simulation and -39 Sv with a standard deviation of 5 Sv for the filtered one. The unfiltered simulation is closer to the observed value of 48.8 Sv (Reynaud et al. 1995), which suggests that the unfiltered simulation is more realistic. Overall, removal of high-frequency atmospheric phenomena decreased the mean gyre strength by about 25% from 2002 to 2010. Since Condron and Renfrew (2013) found that polar lows caused the gyre to spin up by 3.9%, our result highlights the importance of a wider range of atmospheric phenomena to the circulation of the North Atlantic.

While it is not surprising that the strength of the wind-driven gyre decreased in response to a decrease of both wind stress and buoyancy loss at the surface, our result is significantly larger than the estimate of Jung et al. (2014), who found that incorporating high-frequency atmospheric phenomena increased the gyre strength by about 10%. There are several reasons for the significant differences

TABLE 1. The mean and std dev of the AMOC at 26.5°N observed from 2 Apr 2004 to 10 Apr 2008 (Rayner et al. 2011) compared with the ANHA4 simulations.

RAPID	Unfiltered	Filtered	CORE-II
$18.8 \pm 4.8 \text{ Sv}$	$27.4 \pm 4.3 \text{ Sv}$	$20.5 \pm 2.5 \text{ Sv}$	$23.5 \pm 5.0 \text{ Sv}$

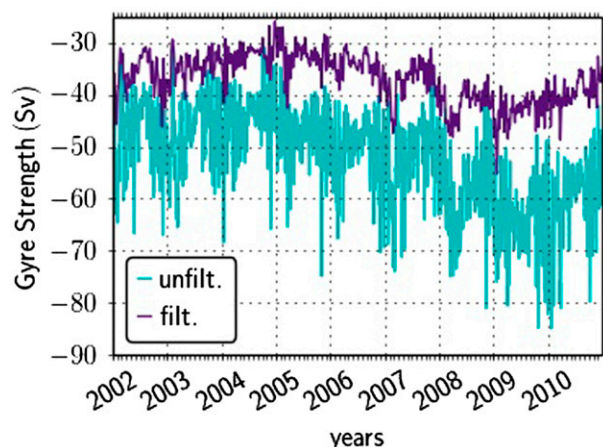


FIG. 7. Max subpolar gyre strength computed from the barotropic streamfunction.

between our results and theirs for both the AMOC and the gyre strength. While their study was restricted to mesoscale geometries, ours includes synoptic-scale forcing. And, as alluded to in the introduction, the European Centre for Medium-Range Weather Forecasts (ECMWF) forcing dataset used in their study has a temporal resolution that is insufficient to capture high-frequency variability near the poles. In addition, their coarse-resolution model may have resolved some of the high-frequency

forcing that we have removed with our filter so the effects of these phenomena would not have been captured by their coarse-graining comparisons.

Weakening of the subpolar gyre necessarily led to a decrease in the amount of eddies in the Labrador Sea through a corresponding decrease of shear instability. Furthermore, decreasing the wind stress also generated less turbulent mixing. Thus, we expect an analogous decrease in the eddy kinetic energy (EKE). Figure 8 shows the average surface EKE represented as a speed $\sqrt{2EKE}$ for each of the ANHA4 simulations. The CORE-II output only extends to 2008 so we computed the average from 2002 to 2008. The CORE-II and filtered runs had a similar structure to the surface EKE produced from NCEP-NCAR reanalyses (Luo et al. 2014). But the surface EKE produced from the CGRF dataset was noticeably more detailed in structure, demonstrating that without high-frequency wind and temperature phenomena the localized turbulent mixing is not well represented. Consequently, the plot of EKE averaged over the 3000-m isobath of the Labrador Sea shown in Fig. 8d indicates that the filtered atmospheric forcing data produced about 75% less eddy kinetic energy in the Labrador Sea compared with the unfiltered forcing dataset. In agreement with the results presented so far, the plot shows that fluctuations increased significantly in the presence of high-frequency forcing.

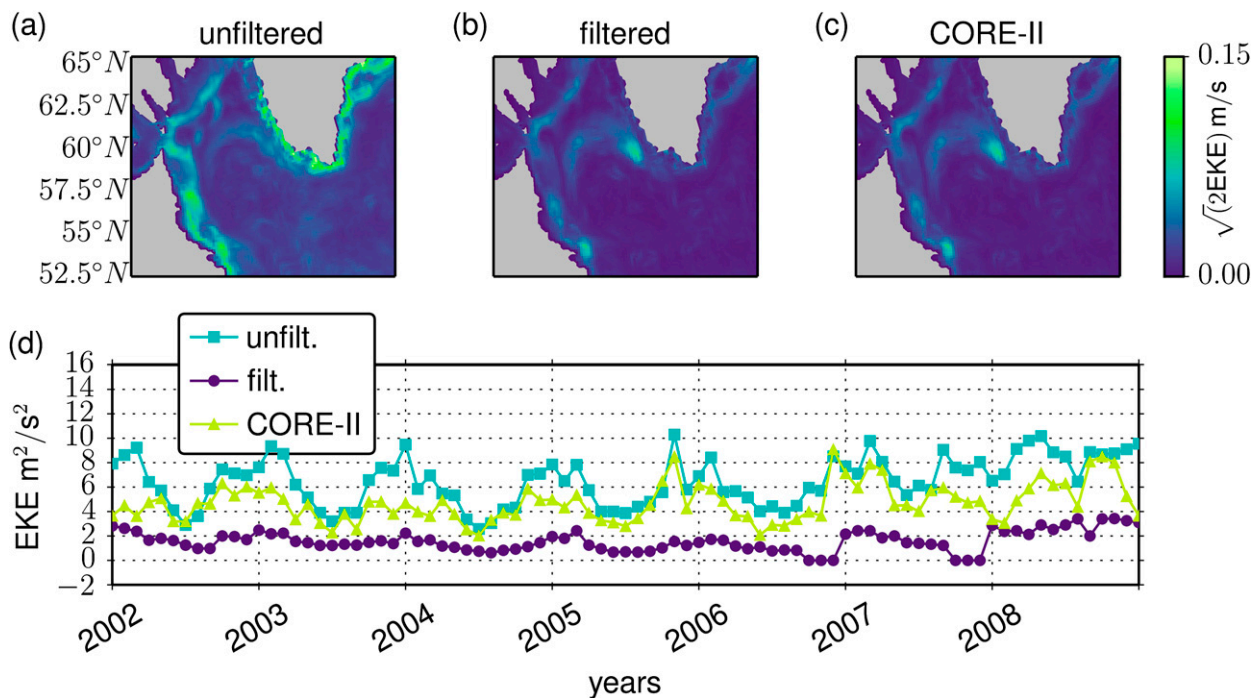
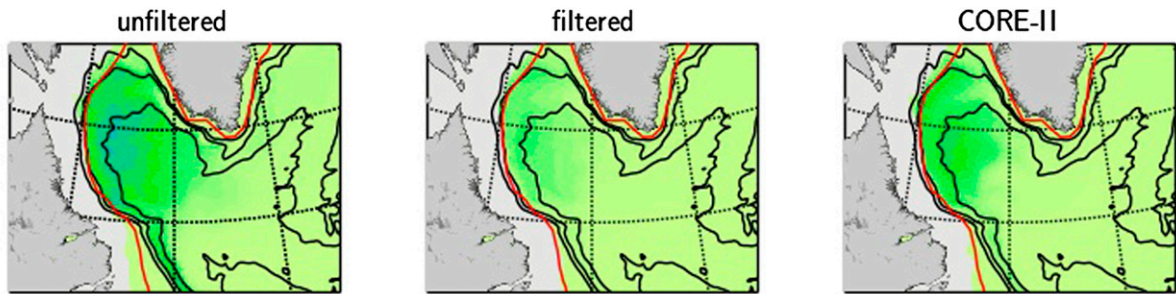
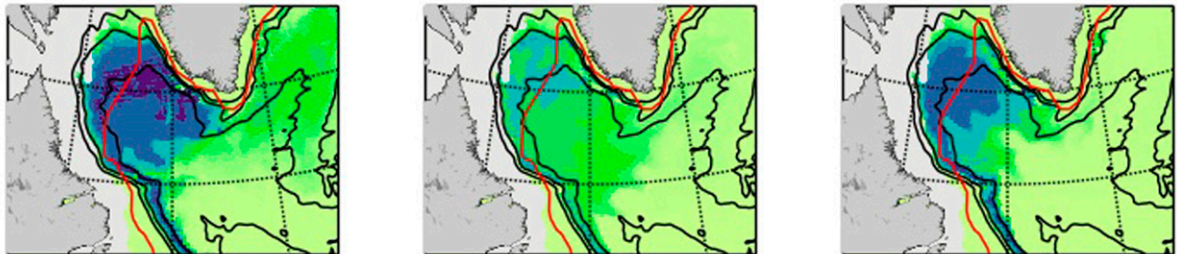


FIG. 8. (a)–(c) Surface EKE averaged over 2002–08 with the same color scale. (d) Monthly mean EKE over the 3000-m isobath of the Labrador Sea ($\lambda \leq 44^\circ W$).

(a) Average 2002-2008 (Feb.– Apr.)



(b) March 10, 2008



(c) April 8, 2003

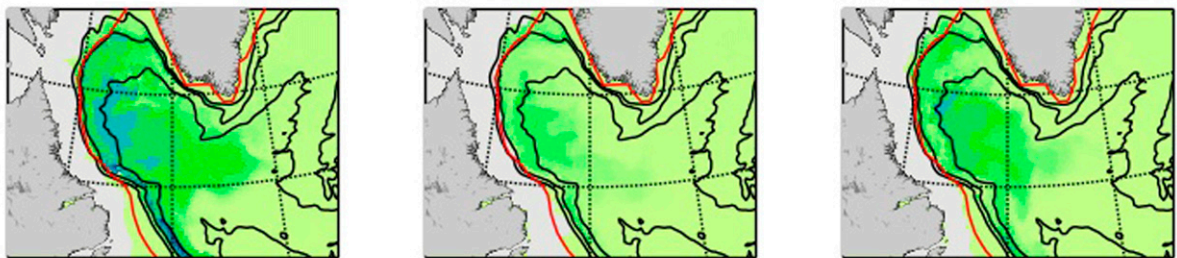


FIG. 9. MLDs within the Labrador Sea (a) on average and on the day that convection reached an annual max in (b) 2008 and (c) 2003. The black contours that indicate depth and the dotted lines that indicate latitude are labeled as in Fig. 1b. The model sea ice extent is shown in white and the observed sea ice extent is shown with a red line.

b. Deep convection

There are remarkable differences in the depth and the lateral extent of convection among the three different simulations. However, before we proceed to make direct comparisons between the models, we will discuss the models' representation of convection in the Labrador Sea to make it clear that these limitations do not obfuscate comparisons between them. Figure 9 shows the depth of the mixed layer and sea ice extent in the Labrador Sea for the CGRF, filtered CGRF, and CORE-II simulations. The model sea ice extent is shown in white and, for comparison, the weekly mean sea ice extent derived from observational data is shown with a red line (Reynolds et al. 2002). The model generally does a good job of representing sea ice in the Labrador Sea with the exception of the winter of 2007/08 during which the sea ice extent was underpredicted. Without this ice cover,

we expect greater heat fluxes out of the sea in our model during that winter than occurred in reality (Griffies et al. 2009), which helps to explain why mixing occurs so broadly in Fig. 9b. Overall, the lateral area of convection is somewhat larger than observations as illustrated, for example, by comparing Fig. 9a, which shows the mixed layer depth averaged over 2002–08, with Våge et al. (2009) (Fig. 2). Salinity drift is known to be a limitation of these models (Rattan et al. 2010), which is likely responsible for the unrealistic area of mixing. However, the lateral area and maximum depth of convection varies in response to changes in atmospheric forcing, which implies that changes in the mixed layer between the different simulations are driven by the atmospheric forcing fields. Even though the lateral area and depth of mixing in the models are not representative of the observations, the model response is consistent among all of the ANHA4 simulations. Thus, relative comparisons

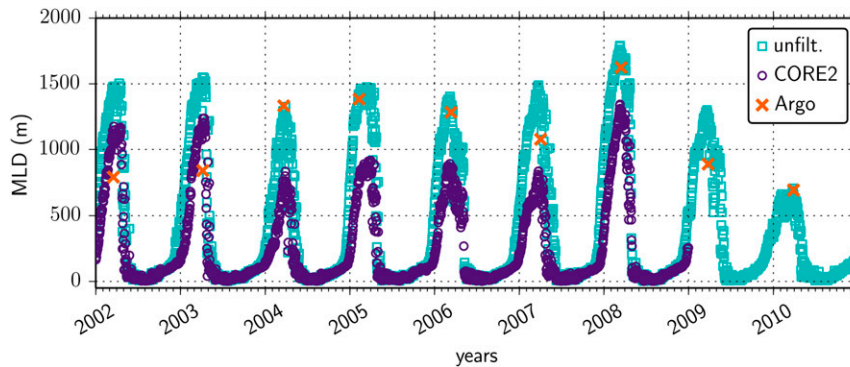


FIG. 10. Daily MLDs averaged within the 3000-m isobath of the Labrador Sea ($\lambda \leq 44^\circ\text{W}$). Argo values represent the max depth measured by an Argo float for each year.

between the model outputs provide a realistic indicator of the response of the ocean to high-frequency atmospheric forcing.

Figure 9a shows that the deepest mixing occurs along the 3000-m isobaths running from 55° to 60°N . Figure 9c shows similar behavior for the winter of 2002/03 with convection stretching farther to the south. Generally, the location of convection in our model is consistent with other model studies (Luo et al. 2014; Jung et al. 2014; Saenko et al. 2014). The deepest mixing occurs somewhat farther north than observations indicate, but this can be explained by considering that the models do not properly represent the physical role of eddies at this resolution (Saenko et al. 2014). Moore et al. (2014) conjectured that the location of deepest convection is influenced by oceanic preconditioning as well as by high-frequency forcing events. This is confirmed by Fig. 9, which shows that the locations of deepest convection differ between the filtered and unfiltered simulations.

Mixed layer depths are plotted for the CGRF and CORE-II simulations in Fig. 10. For comparison, we found the maximum depth obtained from an Argo float profile for each year from a collection of floats in the central Labrador Sea with depths $\geq 3000\text{m}$. The Argo program started in 2002 having fewer floats and some issue with drifting sensors, but float reliability has steadily improved over the years (Roemmich et al. 2009). For each year, the number of relevant profiles is given in Table 2. Both simulations reproduced the observed annual pattern of mixed layer deepening throughout the winter followed by a rapid restratification that leads to shallow MLDs throughout spring and summer (Yashayaev and Loder 2009). The day that the average MLD reached its annual maximum and the restratification of the water column began occurred between the beginning of March and the end of April depending upon the year of the simulation. In comparison with the Argo data, the unfiltered CGRF

simulations generally produced more realistic MLDs than the CORE-II simulations.

The role that high-frequency atmospheric forcing plays in deep convection can be understood by examining changes in ocean stratification between the different simulations. Figure 11a shows that the average MLD was greater for the unfiltered simulation than it was for the filtered simulation throughout the entire record. The maximum average MLD increased by 70% (about 540 m) on average from 2002 to 2010 across all of the years with an increase as large as 110% in 2010 and as low as 20% in 2008. Figure 2 shows that, relative to the period 2002–10, 2010 exhibited the warmest winter temperatures, while 2008 was persistently cold throughout the winter. High-frequency atmospheric forcing had the greatest impact on mixed layer deepening in years that wintertime temperatures were moderate to weak and less of an impact in years with a relatively greater number of extremely cold days.

Varying as a function of the stability of the water column, the convective energy, shown in Fig. 11b, reached its annual minimum around the same time that the mixed layer reached its annual maximum. To a depth of 750 m the filtered simulation had higher CE in winter and, therefore, increased stability of the water column. Of course, this was the expected result corresponding to the aforementioned increase in heat loss and eddy kinetic energy associated with high-frequency forcing. In the summer, the unfiltered simulation had a more stable stratification than the filtered simulation. Storms mix buoyancy inputs such as freshwater throughout the upper ocean. Hence, with fewer storms the filtered simulation

TABLE 2. The number of ARGO profiles within the 3000-m isobath of the Labrador Sea ($\lambda \leq 44^\circ\text{W}$) for each year.

2002	2003	2004	2005	2006	2007	2008	2009	2010
263	456	568	584	774	949	975	1391	1581

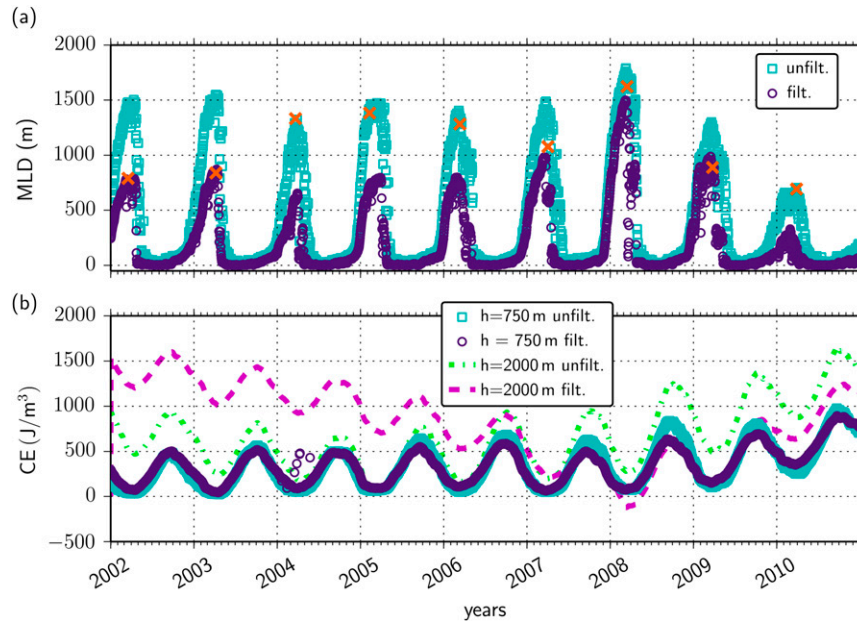


FIG. 11. Daily average taken within the 3000-m isobath of the Labrador Sea ($\lambda \leq 44^\circ\text{W}$) for (a) the MLD and (b) CE [Eq. (3)].

had a weaker stratification within the upper 750 m. Near the end of summer, MLDs reached their annual minimum and the CE reached an annual maximum. During this period, the unfiltered simulation was marked by episodes of localized mixed layer deepening that weakened the stratification thereby preconditioning the Labrador Sea for deep convection.

Over greater depths, the difference between the two simulations was much more pronounced. The convective energy for the unfiltered run decreased from 2002 to 2008, becoming negative during the winter of 2008 and increasing in subsequent years. Figure 2 shows that the year 2008 was particularly cold. Periods of persistent and extreme cold temperatures facilitated a relatively high loss of buoyancy at the surface shown in Fig. 5—high enough that, even in the absence of high-frequency forcing and the accompanied negative temperature anomalies, surface waters increased in density until the water column became unstable.

The unfiltered data produced much greater MLDs than both the CORE-II and the filtered simulations. Figure 9 compares snapshots of the MLDs on the day that convection reached an annual maximum for 2003 and 2008. These are the years when the difference between the maximum MLD in the unfiltered and filtered runs was at a maximum (Fig. 9b) and a minimum (Fig. 9c). The deep convecting region for the filtered run had a relatively small area and depth compared to the unfiltered run for both years. What is more, animations of MLDs (not shown) demonstrated that the depth and shape of

the convective region changed on a daily time scale with less variability when high-frequency atmospheric forcing had been removed.

Figure 12a shows that the filtered simulation had a relatively high freshwater content during the spring and summer when MLDs were relatively shallow. This can be explained by considering that freshwater from melting ice reaches the Labrador Sea around this time and, in the absence of mixing, remains at the surface. The mean heat content increased by about 82% in the absence of high-frequency atmospheric phenomena, as shown in Fig. 12b. This is a consequence of the reduction in sensible and latent heat fluxes, as well as a reduction in the eddy kinetic energy that mixes the heat and freshwater contents from the upper layer.

c. Wind versus temperature

The wind and temperature fields are inexorably connected because of their influence on sensible and latent heat fluxes. Nonetheless, there is still some question as to the relative contributions of each field to the oceanic response. Therefore, two additional simulations were run that mirrored the filtered run, but one was forced with filtered winds and unfiltered temperatures and the other with filtered temperatures and unfiltered winds.

Figure 13 shows that the maximum depth of convection was greater when the temperature anomalies were filtered, but wind anomalies remained. Moreover, the MLD from the wind-filtered simulation resembled those of the filtered simulation in Fig. 11 whereas the temperature-filtered

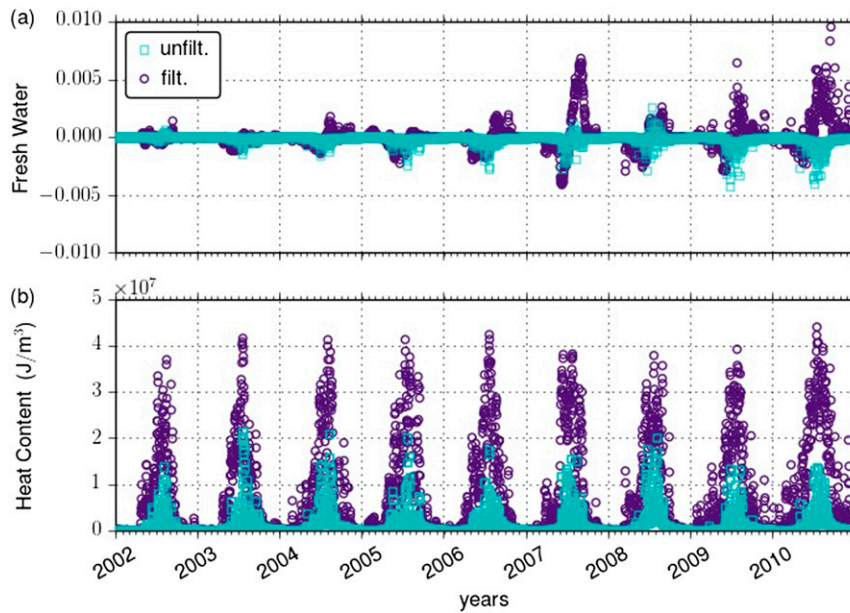


FIG. 12. Averages taken within the mixed layer of the 3000-m isobath of the Labrador Sea ($\lambda \leq 44^\circ\text{W}$) of (a) freshwater content and (b) heat content.

simulation matched more closely with the unfiltered simulation. Hence, perturbations of the wind field have a greater influence on the annual maximum depth of convection than perturbations in temperature, which is not surprising considering that the wind mixes the ocean directly as well as influencing heat fluxes through the bulk formula. In spite of this, high-frequency temperature

anomalies impacted the stratification of the Labrador Sea. For example, the negative CE (in 2000) shown in Fig. 13b could only be reproduced by the wind-filtered run and not the temperature-filtered run. Even though wind perturbations weakened the stratification, the presence of temperature anomalies changed the stratification from weak to unstable. While the filter did not

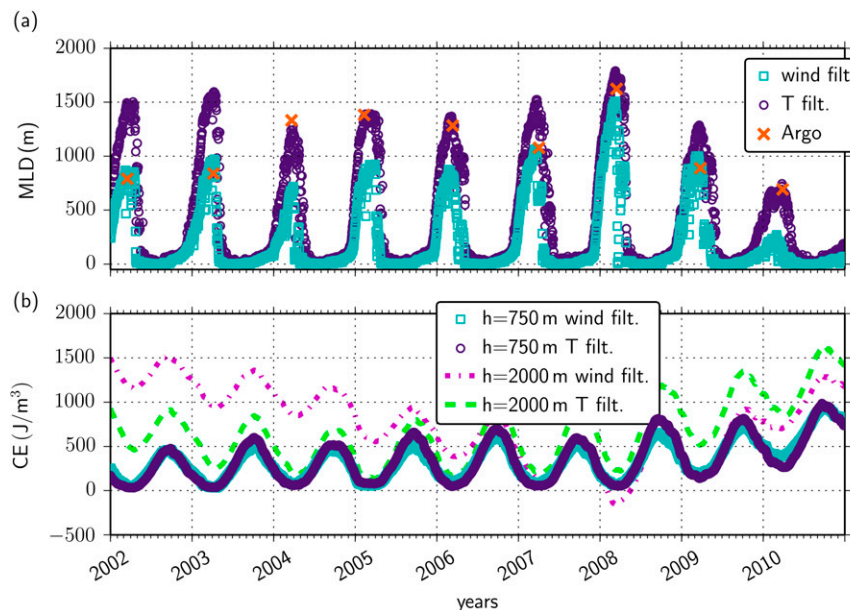


FIG. 13. The relative contribution of the high-frequency wind and temperature perturbations to the stratification within the 3000-m isobath of the Labrador Sea ($\lambda \leq 44^\circ\text{W}$). Daily averages are shown for (a) the MLD and (b) CE [Eq. (3)].

reduce the mean T , it noticeably reduced the finescale variability as shown by Figs. 2e and 2f. This suggests that short-time-scale perturbations in temperature due to, for example, cold air outbreaks play a nonnegligible role in setting the stratification.

All of the simulations exhibited deep mixed layers during the winters of 2007/08 and 2008/09. In years with relatively small negative heat fluxes (Fig. 5), high-frequency winds had a more significant effect on mixed layer deepening than high-frequency temperatures did.

5. Conclusions

High-frequency atmospheric forcing phenomena such as fronts, storms, cold air outbreaks, barrier winds, and topographic jets were found to increase the circulation of the North Atlantic by about 25% through their influence on the AMOC and the subpolar gyre. Whether this is simply due to a reduction in wind stress that decreases the magnitude of heat fluxes and EKE or, in part, to entrainment and mixing resulting from storms is a subject that deserves closer investigation.

The removal of high-frequency atmospheric phenomena was found to reduce the variability in the strength of the AMOC and subpolar gyre. Thus, we provided evidence that high-frequency atmospheric forcing produces episodic fluctuations in the AMOC and the subpolar gyre strength. However, the relative contribution of the various atmospheric phenomena studied here remains unclear.

Without high-frequency atmospheric forcing, the density stratification in the Labrador Sea was more stable. These changes in stratification are intrinsically linked to the eddy kinetic energy of the Labrador Sea, which decreased by about 75% in response to decreases in both the wind-driven circulation and the turbulent kinetic energy. In consequence, high-frequency phenomena were found to strongly influence the depth and lateral extent of deep convection in the Labrador Sea from 2002 to 2010 increasing maximum mixed layer depths by 20% in relatively cold years and as much as 110% in warmer years. In extremely cold years, such as 2008, mixed layer deepening can extend to extreme depths (≥ 2000 m) in the model even in the absence of high-frequency forcing, whereas in relatively warm years it had a greater influence on the maximum depth of convection.

If, as predicted, the number of polar lows annually decreases as atmospheric temperatures rise (Zahn and von Storch 2010), then knowing the role that high-frequency atmospheric phenomena play in deep convection will improve our understanding of the long-term consequences of changing atmospheric conditions on general ocean circulation.

High-frequency perturbations of the wind field had a greater impact than high-frequency perturbations of temperature. This was expected because the removal of the wind stress lowers the eddy kinetic energy and, more importantly, reduces the latent and sensible heat fluxes.

We have presented evidence that high-frequency forcing is vital to the deep convection of the Labrador Sea and to the circulation of the North Atlantic. Therefore, changes in high-frequency forcing are expected to significantly influence global ocean circulation.

The work presented here highlights the need for a closer examination of the influence of high-frequency atmospheric phenomena on subsurface ocean processes. And given the impact of high-frequency forcing on the circulation of the ocean, a study of synoptic-scale forcing is also warranted. Since the removal of high-frequency forcing necessarily reduced the mean climatological values, the question posed by Marshall and Schott (1999) of whether or not powerful short-time-scale events have the same effect on convection if distributed evenly over the winter months still remains. The fact that the mean value of the temperature did not significantly change when filtered, although there was a noticeable effect on stratification due to temperature anomalies, provides a clue that the localized impact of high-frequency forcing may be important, but a complete investigation is left for an independent study.

Acknowledgments. The authors thank Greg Smith for providing the CGRF data, Xianmin Hu for his help with the model, and Andrew Roberts for helpful discussions. We also thank the three reviewers of our manuscript whose comments improved its overall quality. We acknowledge funding from NSERC through the VITALS network (Award 433898-2012).

GLORYS reanalysis received support from INSU-CNRS, Mercator Océan, Groupe Mission Mercator Coriolis, and the European Community's Seventh Framework Programme FP7/2007-2013 under Grant Agreement number 218812 (MyOcean).

The Argo float data used in this paper were collected and made freely available by the International Argo Program and the national programs that contribute to it (<http://www.argo.ucsd.edu> and <http://www.jcommops.org/argo>). The Argo Program is part of the Global Ocean Observing System.

Data from the RAPID-WATCH MOC monitoring project are funded by the Natural Environment Research Council and are freely available from www.rapid.ac.uk/rapidmoc.

The CORE.2 Global Air–Sea Flux Dataset is available from the Research Data Archive at the National Center for Atmospheric Research, Computational and

Information Systems Laboratory (<http://dx.doi.org/10.5065/D6WH2N0S>; Yeager and Large 2008). It was accessed 4 November 2014.

NOAA_OI_SST_V2 data are provided by the NOAA/OAR/ESRL PSD, Boulder, Colorado, USA, from their Web site (<http://www.esrl.noaa.gov/psd/>). The data were accessed 7 January 2013.

APPENDIX

Wavelet Power Spectra

The continuous wavelet transform of a signal $s(t)$ is given by

$$\tilde{s}(a, b) = \int_{-\infty}^{+\infty} s(t) \bar{Y}_{a,b}(t) dt, \quad (\text{A1})$$

where

$$\bar{Y}_{a,b}(t) = \frac{1}{\sqrt{a}} \bar{Y}\left(\frac{t-b}{a}\right) \quad (\text{A2})$$

and $\bar{Y}(t)$ is the complex conjugate of the “mother wavelet” $Y(t)$. For scale a at time b the wavelet bases are dilations and translations of the mother wavelet. The wavelet scale can be related analytically to the Fourier period to determine Fourier modes. Wavelet coefficients $\tilde{s}(a, b)$ are determined using wavelet basis functions.

The wavelet power spectrum, also known as the scalogram, is defined as the squared absolute value of the wavelet coefficient:

$$P(a, b) = |\tilde{s}(a, b)|^2. \quad (\text{A3})$$

The choice of mother wavelet depends both on the applications and on the signal being analyzed. Wavelet bases can be real or complex, contain variable numbers of vanishing moments, and vary in shape. While real wavelets capture both positive and negative oscillations of a signal, complex wavelets combine positive and negative oscillations into a single broad peak. In addition, our forcing data contain many oscillations so the appropriate wavelet should reflect that.

We chose to use the Morlet wavelet defined by the mother wavelet:

$$\psi_0(t) = \pi^{-1/4} e^{-t^2/2} e^{i\omega_0 t}, \quad (\text{A4})$$

with $\omega_0 = 6$. This implies a Fourier period of $\lambda \simeq 1.03$ (Torrence and Compo 1998), which allows for a straightforward conversion between scale and period. The Morlet wavelet provides excellent frequency resolution although it is at the expense of temporal

resolution. This trade-off is near-optimal for scalograms, but a better temporal resolution would be needed to analyze the local structure.

To find the wavelet power spectrum we adapted the online wavelet toolbox provided by Torrence and Compo (1998). The open-source toolbox is freely available and is well tested (Linkenkaer-Hansen et al. 2001; Moy et al. 2002; Holdsworth et al. 2012). Our data were first normalized by subtracting its mean and dividing by its standard deviation. To determine which elements of the spectrum were most significant we computed the expected value for Gaussian red noise and compared it to our signal. This provides a useful diagnostic for noisy data since we can say, with 95% confidence, that the part of the wavelet power spectrum above the red noise contour is significant (i.e., not due simply to noisy fluctuations). We plot this 95% confidence contour on all scalogram plots to identify the most significant features with a black contour line.

REFERENCES

- Amante, C., and B. W. Eakins, 2009: ETOPO1 1 arc-minute global relief model: Procedures, data sources and analysis. NOAA Tech. Memo. NESDIS NGDC-24, 19 pp.
- Avsic, T., J. Karstensen, U. Send, and J. Fischer, 2006: Interannual variability of newly formed Labrador Sea Water from 1994 to 2005. *Geophys. Res. Lett.*, **33**, L21S02, doi:10.1029/2006GL026913.
- Azetsu-Scott, K., E. P. Jones, I. Yashayaev, and R. M. Gershey, 2003: Time series study of CFC concentrations in the Labrador Sea during deep and shallow convection regimes (1991–2000). *J. Geophys. Res.*, **108**, 3354, doi:10.1029/2002JC001317.
- Bailey, D. A., P. B. Rhines, and S. Häkkinen, 2005: Formation and pathways of North Atlantic Deep Water in a coupled ice–ocean model of the Arctic–North Atlantic Oceans. *Climate Dyn.*, **25**, 497–516, doi:10.1007/s00382-005-0050-3.
- Barnier, B., and Coauthors, 2007: Eddy-permitting ocean circulation hindcasts of past decades. *CLIVAR Exchanges*, No. 42, International CLIVAR Project Office, Southampton, United Kingdom, 8–10.
- Condran, A., and I. A. Renfrew, 2013: The impact of polar meso-scale storms on northeast Atlantic Ocean circulation. *Nat. Geosci.*, **6**, 34–37, doi:10.1038/ngeo1661.
- , G. R. Bigg, and I. A. Renfrew, 2006: Polar mesoscale cyclones in the northeast Atlantic: Comparing climatologies from ERA-40 and satellite imagery. *Mon. Wea. Rev.*, **134**, 1518–1533, doi:10.1175/MWR3136.1.
- Dai, A., and K. E. Trenberth, 2002: Estimates of freshwater discharge from continents: Latitudinal and seasonal variations. *J. Hydrometeor.*, **3**, 660–687, doi:10.1175/1525-7541(2002)003<0660:EOFDFC>2.0.CO;2.
- Eskridge, R. E., J. Y. Ku, S. T. Rao, P. S. Porter, and I. G. Zurbenko, 1997: Separating different scales of motion in time series of meteorological variables. *Bull. Amer. Meteor. Soc.*, **78**, 1473–1483, doi:10.1175/1520-0477(1997)078<1473:SDSOMI>2.0.CO;2.
- Ferrari, R., and C. Wunsch, 2009: Ocean circulation kinetic energy: Reservoirs, sources, and sinks. *Annu. Rev. Fluid Mech.*, **41**, 253–282, doi:10.1146/annurev.fluid.40.111406.102139.

- Frajka-Williams, E., P. B. Rhines, and C. C. Eriksen, 2014: Horizontal stratification during deep convection in the Labrador Sea. *J. Phys. Oceanogr.*, **44**, 220–228, doi:10.1175/JPO-D-13-069.1.
- Griffies, S. M., and Coauthors, 2009: Coordinated Ocean–Ice Reference Experiments (COREs). *Ocean Modell.*, **26**, 1–46, doi:10.1016/j.ocemod.2008.08.007.
- Gulev, S. K., O. Zolina, and S. Grigoriev, 2001: Extratropical cyclone variability in the Northern Hemisphere winter from the NCEP/NCAR reanalysis data. *Climate Dyn.*, **17**, 795–809, doi:10.1007/s003820000145.
- Hallberg, R., 2013: Using a resolution function to regulate parameterizations of oceanic mesoscale eddy effects. *Ocean Modell.*, **72**, 92–103, doi:10.1016/j.ocemod.2013.08.007.
- Holdsworth, A. M., N. K.-R. Kevlahan, and D. J. D. Earn, 2012: Multifractal signatures of infectious diseases. *J. Roy. Soc. Interface*, **9**, 2167–2180, doi:10.1098/rsif.2011.0886.
- Hunke, E. C., and W. H. Lipscomb, 2008: CICE: The Los Alamos sea ice model, documentation and software user's manual, version 4.0. Los Alamos National Laboratory Tech. Rep. LA-CC-06-012, 59 pp.
- Ibarra-Berastegi, G., I. Madariaga, A. Elías, E. Agirre, and J. Uria, 2001: Long-term changes of ozone and traffic in Bilbao. *Atmos. Environ.*, **35**, 5581–5592, doi:10.1016/S1352-2310(01)00210-2.
- Jung, T., S. Serrar, and Q. Wang, 2014: The oceanic response to mesoscale atmospheric forcing. *Geophys. Res. Lett.*, **41**, 1255–1260, doi:10.1002/2013GL059040.
- Kuhlbrodt, T., A. Griesel, M. Montoya, A. Levermann, M. Hofmann, and S. Rahmstorf, 2007: On the driving processes of the Atlantic meridional overturning circulation. *Rev. Geophys.*, **45**, RG2001, doi:10.1029/2004RG000166.
- Large, W. G., and S. G. Yeager, 2004: Diurnal to decadal global forcing for ocean and sea-ice models: The data sets and flux climatologies. NCAR Tech. Note NCAR/TN-460+STR, 105 pp., doi:10.5065/D6KK98Q6.
- , and —, 2009: The global climatology of an interannually varying air–sea flux data set. *Climate Dyn.*, **33**, 341–364, doi:10.1007/s00382-008-0441-3.
- Lazier, J. R., 1980: Oceanographic conditions at ocean weather ship Bravo, 1964–1974. *Atmos.–Ocean*, **18**, 227–238, doi:10.1080/07055900.1980.9649089.
- , R. Hendry, A. Clarke, I. Yashayaev, and P. Rhines, 2002: Convection and restratification in the Labrador Sea, 1990–2000. *Deep-Sea Res. I*, **49**, 1819–1835, doi:10.1016/S0967-0637(02)00064-X.
- Lilly, J. M., P. B. Rhines, F. Schott, K. Lavender, J. Lazier, U. Send, and E. D'Asaro, 2003: Observations of the Labrador Sea eddy field. *Prog. Oceanogr.*, **59**, 75–176, doi:10.1016/j.pocean.2003.08.013.
- Linkenkaer-Hansen, K., V. Nikouline, J. Palva, and R. Ilmoniemi, 2001: Long-range temporal correlations and scaling behavior in human brain oscillations. *J. Neurosci.*, **21**, 1370–1377.
- Luo, H., A. Bracco, and F. Zhang, 2014: The seasonality of convective events in the Labrador Sea. *J. Climate*, **27**, 6456–6471, doi:10.1175/JCLI-D-14-00009.1.
- Madec, G., 2008: NEMO ocean engine. Note du Pôle de modélisation de l'Institut Pierre-Simon Laplace 27, 357 pp.
- Marshall, J., and F. Schott, 1999: Open ocean convection: Observations, theory, and models. *Rev. Geophys.*, **37**, 1–64, doi:10.1029/98RG02739.
- , and Coauthors, 1998: The Labrador Sea deep convection experiment. *Bull. Amer. Meteor. Soc.*, **79**, 2033–2058, doi:10.1175/1520-0477(1998)079<2033:TLSDCE>2.0.CO;2.
- Mellor, G. L., and T. Yamada, 1982: Development of a turbulent closure model for geophysical fluid problems. *Rev. Geophys. Space Phys.*, **20**, 851–875, doi:10.1029/RG020i004p00851.
- Moore, G. W. K., and I. A. Renfrew, 2005: Tip jets and barrier winds: A QuikSCAT climatology of high wind speed events around Greenland. *J. Climate*, **18**, 3713–3725, doi:10.1175/JCLI3455.1.
- , R. S. Pickart, I. A. Renfrew, and K. Våge, 2014: What causes the location of the air–sea turbulent heat flux maximum over the Labrador Sea? *Geophys. Res. Lett.*, **41**, 3628–3635, doi:10.1002/2014GL059940.
- Moy, C. M., G. O. Seltzer, D. T. Rodbell, and D. M. Anderson, 2002: Variability of El Niño–Southern Oscillation activity at millennial timescales during the Holocene epoch. *Nature*, **420**, 162–165, doi:10.1038/nature01194.
- Myers, P. G., and C. Donnelly, 2008: Water mass transformation and formation in the Labrador Sea. *J. Climate*, **21**, 1622–1638, doi:10.1175/2007JCLI1722.1.
- Nikurashin, M., G. K. Vallis, and A. Adcroft, 2013: Routes to energy dissipation for geostrophic flows in the Southern Ocean. *Nat. Geosci.*, **6**, 48–51, doi:10.1038/ngeo1657.
- Overland, J. E., J. M. Adams, and N. A. Bond, 1999: Decadal variability of the Aleutian low and its relation to high-latitude circulation. *J. Climate*, **12**, 1542–1548, doi:10.1175/1520-0442(1999)012<1542:DVOTAL>2.0.CO;2.
- Polo, I., J. Robson, R. Sutton, and M. A. Balmaseda, 2014: The importance of wind and buoyancy forcing for the boundary density variations and the geostrophic component of the AMOC at 26°N. *J. Phys. Oceanogr.*, **44**, 2387–2408, doi:10.1175/JPO-D-13-0264.1.
- Rattan, S., P. G. Myers, A.-M. Treguier, S. Theetten, A. Biastoch, and C. Böning, 2010: Towards an understanding of Labrador Sea salinity drift in eddy-permitting simulations. *Ocean Modell.*, **35**, 77–88, doi:10.1016/j.ocemod.2010.06.007.
- Rayner, D., and Coauthors, 2011: Monitoring the Atlantic meridional overturning circulation. *Deep-Sea Res. II*, **58**, 1744–1753, doi:10.1016/j.dsr2.2010.10.056.
- Reynaud, T. H., A. J. Weaver, and R. J. Greatbatch, 1995: Summer mean circulation of the northwestern Atlantic Ocean. *J. Geophys. Res.*, **100**, 779–816, doi:10.1029/94JC02561.
- Reynolds, R. W., N. A. Rayner, T. M. Smith, D. C. Stokes, and W. Wang, 2002: An improved in situ and satellite SST analysis for climate. *J. Climate*, **15**, 1609–1625, doi:10.1175/1520-0442(2002)015<1609:AIISAS>2.0.CO;2.
- Roberts, A., and Coauthors, 2015: Simulating transient ice–ocean Ekman transport in the Regional Arctic System Model and Community Earth System Model. *Ann. Glaciol.*, **56**, 211–228, doi:10.3189/2015AoS69A760.
- Roemmich, D., and Coauthors, 2009: Argo: The challenge of continuing 10 years of progress. *Oceanography*, **22**, 46–55, doi:10.5670/oceanog.2009.65.
- Saenko, O. A., F. Dupont, D. Yang, P. G. Myers, I. Yashayaev, and G. C. Smith, 2014: Role of resolved and parameterized eddies in the Labrador Sea balance of heat and buoyancy. *J. Phys. Oceanogr.*, **44**, 3008–3032, doi:10.1175/JPO-D-14-0041.1.
- Smith, G. C., F. Roy, P. Mann, F. Dupont, B. Brasnett, J.-F. Lemieux, S. Laroche, and S. Blair, 2014: A new atmospheric dataset for forcing ice–ocean models: Evaluation of reforecasts using the Canadian global deterministic prediction system. *Quart. J. Roy. Meteor. Soc.*, **140**, 881–894, doi:10.1002/qj.2194.
- Smith, S. D., 1988: Coefficients for sea surface wind stress, heat flux, and wind profiles as a function of wind speed and temperature. *J. Geophys. Res.*, **93**, 15 467–15 472, doi:10.1029/JC093iC12p15467.

- Torrence, C., and G. Compo, 1998: A practical guide to wavelet analysis. *Bull. Amer. Meteor. Soc.*, **79**, 61–78, doi:[10.1175/1520-0477\(1998\)079<0061:APGTWA>2.0.CO;2](https://doi.org/10.1175/1520-0477(1998)079<0061:APGTWA>2.0.CO;2).
- Våge, K., and Coauthors, 2009: Surprising return of deep convection to the subpolar North Atlantic Ocean in winter 2007–2008. *Nat. Geosci.*, **2**, 67–72, doi:[10.1038/ngeo382](https://doi.org/10.1038/ngeo382).
- Wise, E., and A. Comrie, 2005: Meteorologically adjusted urban air quality trends in the southwestern United States. *Atmos. Environ.*, **39**, 2969–2980, doi:[10.1016/j.atmosenv.2005.01.024](https://doi.org/10.1016/j.atmosenv.2005.01.024).
- Wunsch, C., and R. Ferrari, 2004: Vertical mixing, energy, and the general circulation of the oceans. *Annu. Rev. Fluid Mech.*, **36**, 281–314, doi:[10.1146/annurev.fluid.36.050802.122121](https://doi.org/10.1146/annurev.fluid.36.050802.122121).
- Xu, X., E. P. Chassignet, W. E. Johns, W. J. Schmitz, and E. J. Metzger, 2014: Intraseasonal to interannual variability of the Atlantic meridional overturning circulation from eddy-resolving simulations and observations. *J. Geophys. Res. Oceans*, **119**, 5140–5159, doi:[10.1002/2014JC009994](https://doi.org/10.1002/2014JC009994).
- Yashayaev, I., and J. W. Loder, 2009: Enhanced production of Labrador Sea Water in 2008. *Geophys. Res. Lett.*, **36**, doi:[10.1029/2008GL036162](https://doi.org/10.1029/2008GL036162).
- Yeager, S. G., and W. G. Large, 2008: CORE.2 Global Air–Sea Flux Dataset. Research Data Archive at the National Center for Atmospheric Research, Computational and Information Systems Laboratory, accessed 4 November 2014, doi:[10.5065/D6WH2N0S](https://doi.org/10.5065/D6WH2N0S).
- Zahn, M., and H. von Storch, 2010: Decreased frequency of North Atlantic polar lows associated with future climate warming. *Nature*, **467**, 309–312, doi:[10.1038/nature09388](https://doi.org/10.1038/nature09388).